

Coseismic ionospheric disturbance of the large strike-slip earthquakes in North Sumatra in 2012: M_w dependence of the disturbance amplitudes

Mokhammad Nur Cahyadi^{1,2} and Kosuke Heki¹

¹Department Natural History Sci., Hokkaido University, Sapporo-city, Hokkaido, Japan. E-mail: cahyadi@geodesy.its.ac.id

²Geomatics Engineering Department, Institut Teknologi Sepuluh Nopember (ITS), Surabaya, Indonesia

Accepted 2014 September 4. Received 2014 September 3; in original form 2014 May 8

SUMMARY

We studied ionospheric responses to the 2012 April 11 M_w 8.6 North Sumatra earthquake using total electron content (TEC) measurements with the regional Global Navigation Satellite System network. This earthquake ruptured the oceanic lithosphere off the Indian Ocean coast of North Sumatra, and is known as the largest strike-slip earthquake ever recorded. Coseismic ionospheric disturbances (CIDs) with rapid TEC enhancement of a few TEC units propagated northward with a speed of acoustic waves ($\sim 1 \text{ km s}^{-1}$). Resonant atmospheric oscillation with a frequency $\sim 4 \text{ mHz}$ have been found as monochromatic oscillation of TEC lasting for an hour after the main shock and the largest aftershock. We compared CID amplitudes of 21 earthquakes world-wide with moment magnitudes (M_w) 6.6–9.2. They roughly obeyed a law such that CID amplitude increases by two orders of magnitude for the M_w increase of three. The 2012 North Sumatra earthquakes slightly deviated negatively from the trend possibly reflecting their strike-slip mechanisms, that is small vertical crustal movements for their magnitudes.

Key words: Acoustic-gravity waves; Ionosphere/atmosphere interactions; Acoustic properties.

1 INTRODUCTION

Global Navigation Satellite System (GNSS) such as the Global Positioning System (GPS) is useful to observe ionospheric total electron content (TEC), number of electrons integrated along the line-of-sight (LOS) connecting the receiver and the satellite. A coseismic ionospheric disturbance (CID) appears shortly after a relatively large earthquake ($M_w \geq 7$) and was first caught with GPS by Calais & Minster (1995). Heki & Ping (2005) performed a comprehensive CID study with a dense GPS array for the 2003 Tokachi-oki earthquake, Japan and investigated propagating velocities and directivities of near-field CID of direct acoustic wave origin. For the 2004 Sumatra–Andaman earthquake (M_w 9.2), Indonesia, Heki *et al.* (2006) used the CID waveform obtained by GPS stations in Indonesia and Thailand to infer the rupture process. Such coseismic disturbances are caused by direct acoustic waves excited at the surface by vertical coseismic crustal movements, but CIDs are also excited by the Rayleigh surface waves and internal gravity waves. A comprehensive review will be available in Tanimoto *et al.* (2014).

After the 2004 Sumatra–Andaman earthquake, two large thrust earthquakes occurred near Sumatra, that is the 2005 Nias (M_w 8.6) and the 2007 Bengkulu (M_w 8.5) earthquakes. Cahyadi & Heki (2013) studied CIDs of the latter with GPS, but found that severe plasma bubble activities masked the CID of the former. They used

GPS data from ~ 20 continuous GPS stations of the Sumatra GPS Array (SUGAR) operated by the Tectonics Observatory of Caltech and the Indonesian Institute of Sciences (LIPI).

On 2012 April 11, an M_w 8.6 intraplate earthquake occurred $\sim 400 \text{ km}$ off the Indian Ocean coast of Northern Sumatra, Indonesia (2.31°N , 93.06°E , focal depth 23 km), at 8:38:37 UT (Meng *et al.* 2012). The largest aftershock (M_w 8.2) occurred $\sim 2 \text{ hr}$ later (10:43:09 UT) $\sim 200 \text{ km}$ southwest of the main shock (0.77°N , 92.45°E , focal depth 16 km). The main shock had a complex source process, that is ruptures of strike-slip mechanism occurred one after another during 160 s on four different sub-faults with a relatively slow rupture velocity (Yue *et al.* 2012). This was the largest strike-slip earthquake ever recorded. Owing to relatively small vertical coseismic crustal movements for strike-slip earthquakes, tsunami height of this earthquake did not exceed 1 m .

In this paper, we investigate the CID of this earthquake using the SUGAR data together with those from several IGS (International GNSS Service) stations. Considering the unique focal mechanism of the 2012 North Sumatra earthquakes, it would be interesting to compare their CID with those of past earthquakes dominated by dip-slip faulting mechanisms. To enable quantitative comparison, we also try to establish an empirical relationship of CID amplitudes with earthquake magnitudes by compiling past examples of CIDs due to earthquakes of various magnitudes.

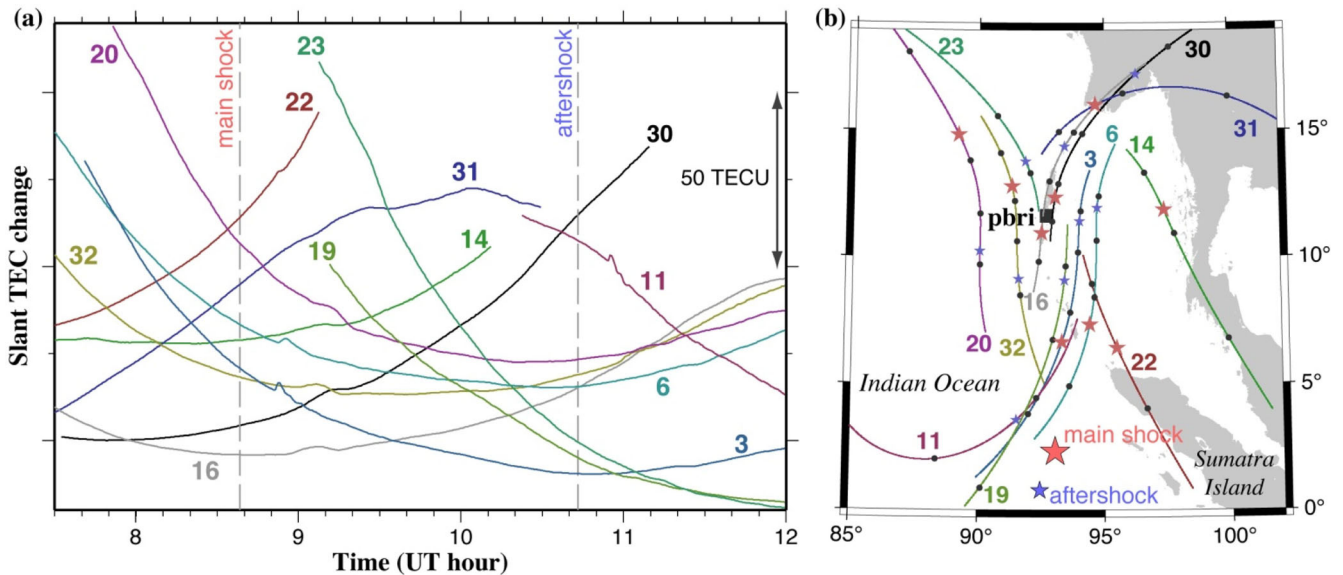


Figure 1. (a) Time-series 07:30–12:00 UT of slant TEC changes observed at the pbri (Port Blair, the Andaman Islands) station (position shown in b) with twelve GPS satellites. Arbitrary biases are added to individual satellites. The two grey dashed vertical lines in (a) indicate the occurrence of the main shock and the largest aftershock of the 2012 North Sumatra earthquake (08:38 and 10:43 UT). CIDs are seen for some of the satellites ~ 10 min after the earthquakes or later. (b) Trajectories of SIP for GPS satellites with hourly time marks (small black dots). On the trajectories, we show SIP positions at 08:38 and 10:43 UT with red and blue stars, respectively. The large red and blue stars are the epicentres of the main shock and the largest aftershock, respectively.

This paper considers CID of the earthquake only, together with its signal propagation, resonant oscillation and directivity; possible pre-seismic signals are discussed elsewhere (Heki & Enomoto 2013).

2 TEC DATA

GPS ground stations receive microwave signals in the two frequencies ~ 1.5 GHz (L1) and ~ 1.2 GHz (L2) transmitted from GPS satellites at altitude of $\sim 20\,200$ km. The microwave signals undergo frequency-dependent delays in the ionosphere. By tracking the differences between the L1 and L2 phases (often called L4), we can monitor the temporal changes of TEC along LOS (called slant TEC). TEC is usually expressed in TECU units (1 TECU corresponds to 10^{16} el m^{-2}). Fig. 1(a) shows slant TEC changes observed at the Port Blair (pbri) station, in the Andaman Islands, ~ 1000 km north of the epicentre, during 07:30–12:00 UT on 12 April 11. Slant TEC shows U-shaped temporal changes due to the apparent movement of GPS satellites in the sky (and consequent changes of the penetration angles of LOS to the ionosphere). When Cahyadi & Heki (2013) studied CIDs of the 2007 Bengkulu earthquake, sampling intervals of the SUGAR stations (2 min) were not sufficiently short for studies of CID whose typical timescale is 4–5 min. In the 2012 data set, however, most stations employed the sampling interval short enough for such studies (15 s).

The coordinates of the ionospheric piercing points (IPP) of LOS were calculated assuming a thin ionosphere at altitude of 300 km (Klobuchar 1987), and the trajectories of their ground projections (subionospheric points, SIP) are plotted on the map in Fig. 1(b). The SIPs of Satellites 3 and 6 were around the middle point between the epicentre and the site when the main shock occurred. In Fig. 1(a), CIDs are visible 10–15 min after the main shock even in the raw slant TEC plots for Satellites 3 and 6. The largest aftershock occurred ~ 2 hr later, and TEC with Satellite 11 shows a clear CID signature.

Slant TEC time-series include long period components coming mainly from the apparent motion of satellites (U-shaped changes),

and partly from latitudinal difference of ionization and slow diurnal change of vertical TEC. We often eliminate them with a high-pass filter by estimating polynomials for vertical TEC and subtract its contributions from the raw data (Ozeki & Heki 2010; Heki 2011). Instead, here we show time-series of vertical TEC (VTEC) in Fig. 2. Accurate conversion from L4 (slant TEC plus biases) to vertical TEC by removing phase ambiguities and interfrequency biases (IFBs) can be done following several steps. We first removed phase ambiguities by comparing them with TEC time-series derived by pseudo-ranges. Then we corrected for satellite IFBs available online from Electronic Navigation Research Institute (ENRI; Sakai 2005). Receiver IFBs were determined to minimize the scatter of night-time VTEC at individual stations, using the approach equivalent to the ‘minimum scalloping’ by Rideout & Coster (2006).

Fig. 2(a) highlights CID, that is N-shaped TEC disturbances appearing 10–15 min after the main shock with amplitudes of a few TECU. Another CID appeared after the largest aftershock (Fig. 2d). These signatures are similar to the case of the 2007 Bengkulu earthquake in southern Sumatra (Cahyadi & Heki 2013). Gentle positive peaks at ~ 11 UT reflect the passage of the IPP across the southern part of equatorial ionization anomaly (compare Figs 2b and c with c), and are not related to the earthquakes. These CIDs can be understood as the ionospheric response to propagating shock-acoustic waves (Afraimovich *et al.* 2001). For the ulmh station data with Satellite 32, TEC showed monochromatic oscillation after the N-shaped disturbances and returned to normal. In this paper, we discuss the initial TEC disturbances and the monochromatic oscillation in Sections 3.2 and 3.3. Stations shown in Fig. 2 have SIPs to the northeast of the epicentre. In Section 3.4, we show that the CIDs have propagated mainly northward from epicentres. Comparative studies of CID amplitudes of various earthquakes will be done in Section 4. In Appendix B (Fig. B1), we show B_z , Dst and K_p over 1-month period including the earthquake. The geomagnetic activity on 12 April 11 was moderately disturbed.

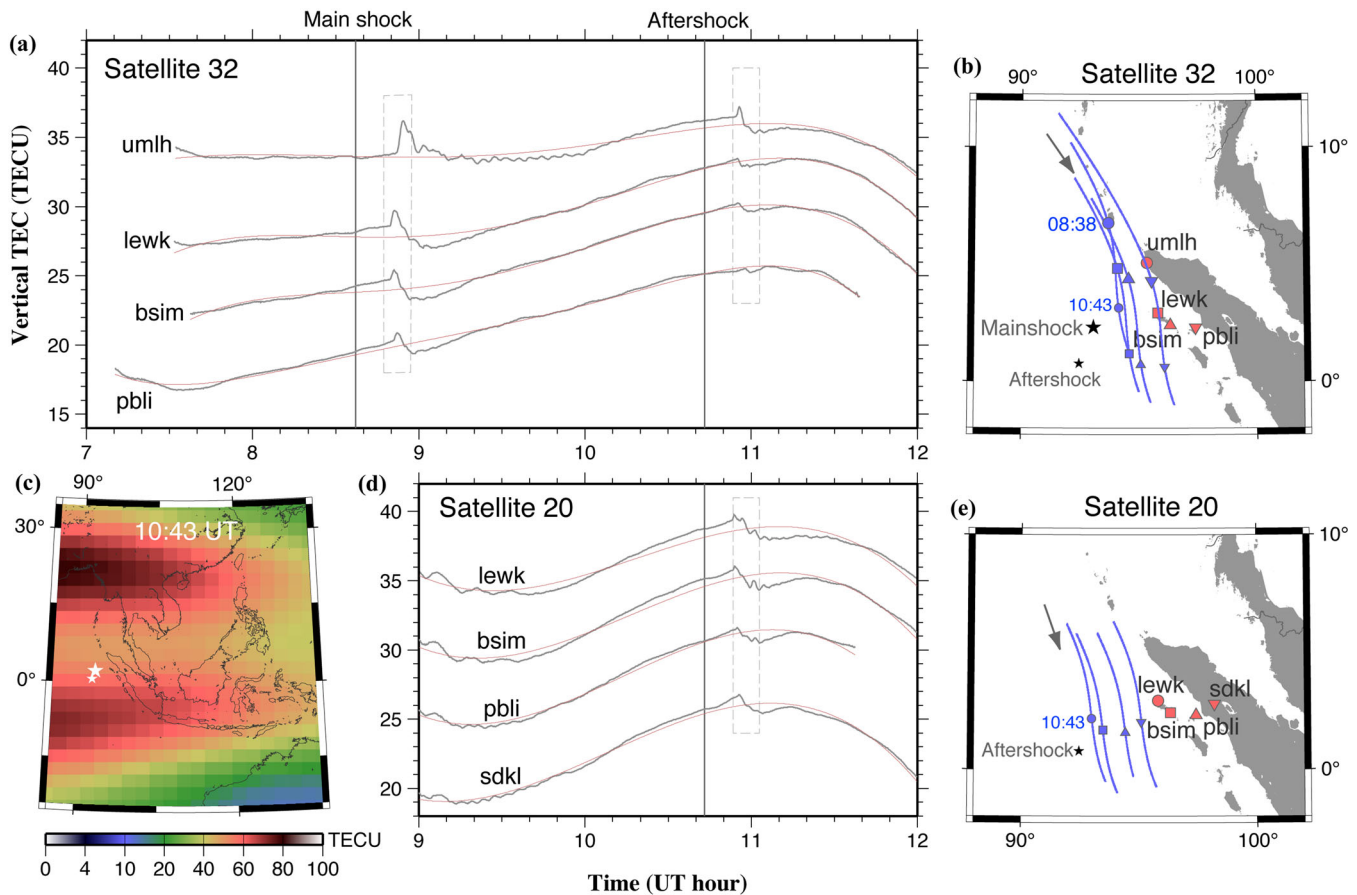


Figure 2. Vertical TEC anomalies recorded at four GPS stations with Satellites 32 (a), and 20 (d). Vertical grey lines are occurrence times of the main shock (08:38 UT) and the largest aftershock (10:43 UT) of the 2012 North Sumatra earthquake. We gave vertical separations 6 TECU between adjacent curves to avoid overlap of the curves. CIDs are seen within the dashed rectangles (10–20 min after earthquakes). Reference curves (thin red) are derived by modelling vertical TEC changes with cubic polynomials of time. Trajectories of SIPs are shown in (b) and (e). Small and large blue circles on the trajectories are SIPs at 08:38 and 10:43 UT, respectively. (c) shows vertical TEC background at 10:43 UT calculated using the Global Ionospheric Map (GIM).

3 NEAR FIELD CID OF THE 2012 NORTH SUMATRA EARTHQUAKE

Fig. 2 in Heki *et al.* (2006) illustrates that earthquakes excite three kinds of atmospheric waves that disturb ionosphere. The fastest and slowest components, induced by the Rayleigh surface wave and the internal gravity wave, respectively, propagate over a long distance. Here we focus on the disturbances caused by direct acoustic waves excited at the surface by coseismic vertical crustal movements. They propagate in near fields, within ~ 1000 km from the epicentres, typically as fast as ~ 0.8 – 1.0 km s^{-1} , depending on time and latitude.

3.1 Coseismic vertical crustal movements

Near field CIDs are excited by coseismic vertical crustal movements. Fig. 3 shows such movements calculated using fault parameters inferred seismologically. Actually, we used geometry and seismic moment of fault segments in fig. 4 of Yue *et al.* (2012). We assumed uniform slips over individual fault segments, and calculated the slips from seismic moments using the rigidity of 50 GPa. We then used the Green's function for an elastic half-space (Okada 1992). The CIDs we found in this study would have been excited by vertical movement of the ocean floor (and hence sea surface) as shown in Fig. 3. In the Appendix A (Fig. A2), we show that even a

pure strike-slip earthquake causes certain amount of vertical crustal movements ($\sim 1/5$ of a dip-slip earthquake of the same magnitude).

3.2 Propagation speed

CIDs are caused by several different atmospheric waves. Ionosphere responses to acoustic waves appear first above epicentres 10–15 min after the main shock as fast ~ 0.8 – 1.0 m s^{-1} . Astafyeva *et al.* (2009) found that CID of the 1994 Hokkaido-Toho-Oki earthquake has two separate components with different propagation speeds. The faster components (~ 4 km s^{-1}) are excited by the Rayleigh surface waves, and propagate farther than those by the direct acoustic waves owing to smaller geometric decay (Rolland *et al.* 2011a). Earthquakes accompanying large tsunamis often show much slower components (~ 0.3 km s^{-1}) caused by internal gravity waves (e.g. Tsugawa *et al.* 2011).

To study the propagation speeds of the CID seen in Fig. 2, we plot the focal distance as a function of time and showed TEC changes with colours in Fig. 4(a) (main shock) and (b) (the largest aftershock). To isolate oscillatory changes with periods of ~ 4 min from TEC time-series, we used the wavelet analysis procedure following Heki & Ping (2005). The propagation speeds after both events were consistent with the sound speed in the F region. Fig. 2(b) appears to show secondary disturbances ~ 10 min after the primary CID.

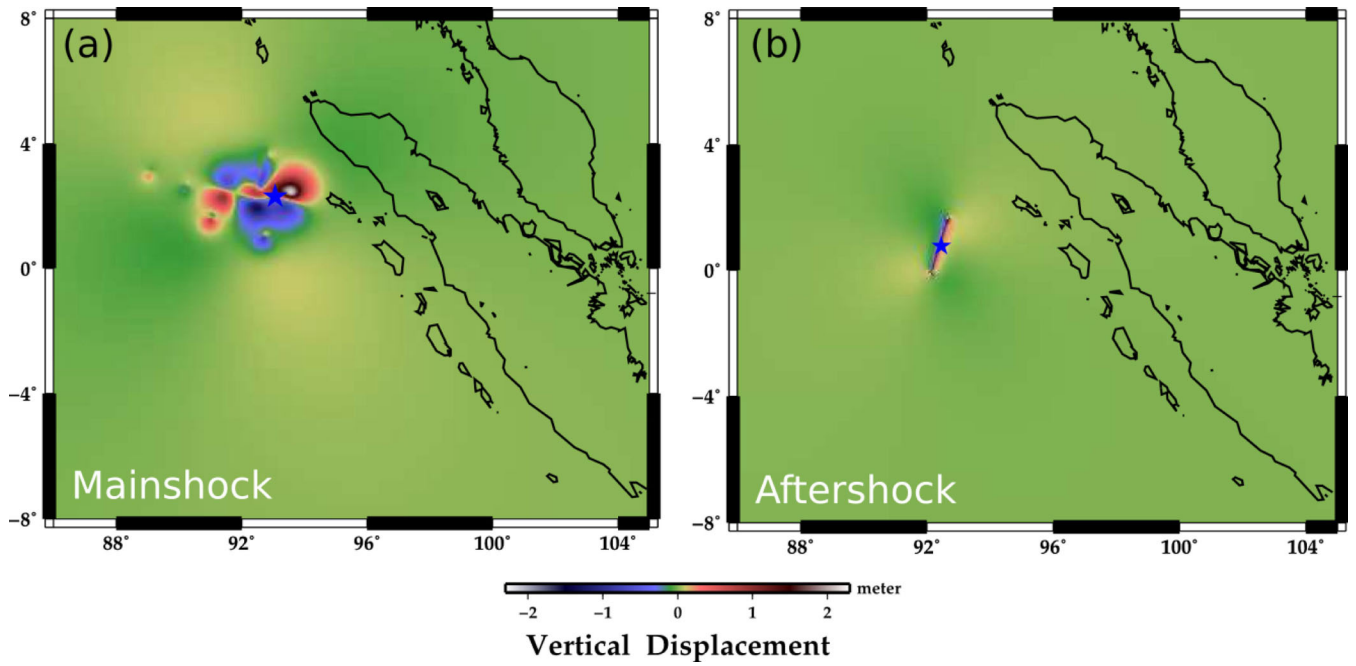


Figure 3. Vertical crustal movements of the main shock (a) and the largest aftershock (b) of the 2012 North Sumatra earthquake. Blue stars show the epicentres of the two earthquakes. They were calculated after Okada (1992), using the fault geometry taken from fig. 4 of Yue *et al.* (2012). Average slips of the four fault segments were inferred from the seismic moments released from the fault segments given there. Although the earthquakes were dominated by the strike-slip mechanism, significant vertical movements occurred. Focal distances in the vertical axes of Fig. 4 are measured from the centres of uplift in this figure.

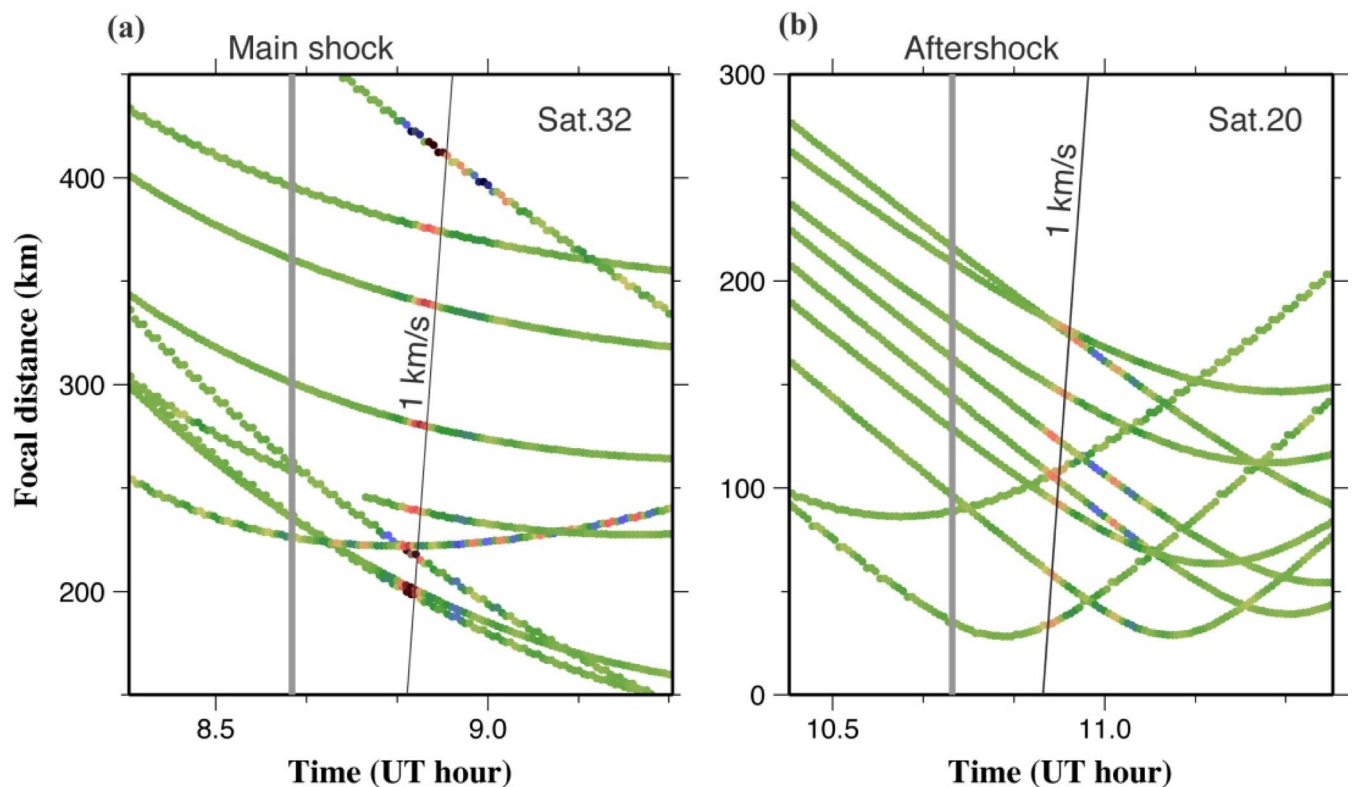


Figure 4. (a) Traveltime diagram of the CID after the 2012 North Sumatra earthquake (main shock) based on the Satellite 32 data. The CID peak (shown in red colours) detected by wavelet propagates with the apparent velocity of $\sim 1 \text{ km s}^{-1}$ (thin black line). Distances are measured from the centre of the uplift (Fig. 3a). The grey vertical line indicates the occurrence of the main shock (08:38 UT). (b) Traveltime diagrams of the largest aftershock CID based on the Satellites 20 data. Distances are measured from the centre of uplift (Fig. 3b). The grey vertical line indicates the occurrence of the aftershock (10:43 UT). Apparent speed is also $\sim 1 \text{ km s}^{-1}$. In both cases, only stations with SIP to the north of the epicentre (i.e. with latitudes higher than the uplift centres) are plotted considering the directivity (Fig. 6).

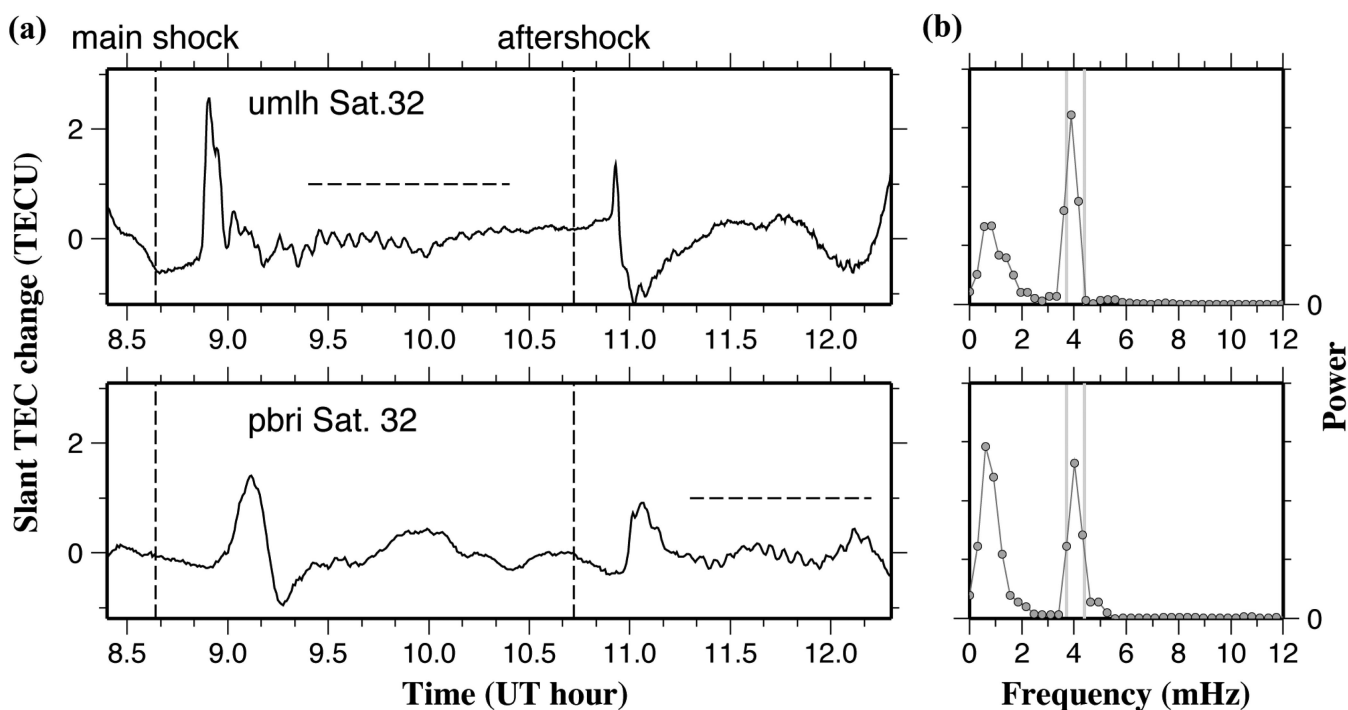


Figure 5. The TEC time-series at umlh (Fig. 2b) and pbri (Fig. 1b) with Satellite 32 show monochromatic oscillation lasting over an hour after the main shock and the largest aftershock, respectively (a). Their spectrograms (b) show peaks around 4 mHz, close to the two atmospheric resonance frequencies 3.7 and 4.4 mHz shown as two vertical lines (Nishida *et al.* 2000). Horizontal dashed lines in (a) show time windows for the spectral analyses.

They are due to incomplete extraction of disturbance signals rather than disturbances by other kinds of atmospheric waves.

3.3 Resonant oscillations

Atmospheric acoustic waves generated by lithospheric and tropospheric phenomena propagate vertically. The waves reflect downward and interfere with the upward propagating waves and cause resonant oscillation (Tahira 1995; Shinagawa *et al.* 2007). Acoustic resonance in 3.7 and 4.4 mHz is found in the Earth's background free oscillation (Nishida *et al.* 2000), and these frequencies were identified in post-seismic monochromatic TEC oscillation by GPS-TEC after the 2004 Sumatra–Andaman earthquake (Choosakul *et al.* 2009), the 2011 Tohoku-oki earthquake (Rolland *et al.* 2011b; Saito *et al.* 2011), and the 2007 Bengkulu earthquake (Cahyadi & Heki 2013). We show spectrograms obtained by the Blackman–Tukey method using the TEC time-series after the main shock and the largest aftershock in Fig. 5. The observed peak frequencies were ~ 4 mHz. This is consistent with the atmospheric resonance frequencies, but relatively short time windows (1 hr in both cases) did not allow more detailed studies, for example which of the two frequencies is closer to the observations.

The visibility of resonant oscillation with TEC would depend on several factors, for example areal extent of the occurrence of the oscillation and the incident angle of the LOS with the wave front. The movement of the neutral atmosphere should also have components parallel with the ambient geomagnetic field in order that the electron may oscillate together (Rolland *et al.* 2011a). Hence, site-satellite pairs showing clear resonant oscillations in TEC need to satisfy all these conditions. Clear signature for the aftershock at pbri with Satellite 32 shows that the oscillation occurred at least ~ 500 km north of the epicentre. However, the oscillation signature was not de-

tectable from pbri after the main shock, when the SIP was ~ 1000 km apart from the epicentre (Fig. 1b).

3.4 Directivity of CID

Heki & Ping (2005) investigated the N–S asymmetry of CIDs of the 2003 Tokachi-oki earthquake, Japan, that is they propagated little toward the north, and attributed it to the geomagnetic field. If particle motions of neutral atmosphere in the F region are perpendicular to the magnetic field, electrons would not move together with neutral particles and the CID would be suppressed. In the mid-latitude region of the Northern Hemisphere, this happens to the north of the epicentre. Recently, Rolland *et al.* (2013) mapped the CID amplitudes and polarities around the epicentre of the 2011 Van earthquake, Turkey. Although Heki & Ping (2005) explained the directivity only in a qualitative manner, Rolland *et al.* (2013) succeeded in reproducing such N–S asymmetry with a realistic simulation.

Although the 2012 North Sumatra earthquakes occurred in the Northern Hemisphere in geographic latitude, their epicentres are located to the south of the magnetic equator. According to the international geomagnetic reference field (IGRF 2010), geomagnetic inclinations above the epicentres of the main shock and the largest aftershock are -14.2° and -17.8° , respectively. Thus it should have the directivity opposite to the Northern Hemisphere, that is southward CID is to be suppressed. Such northward directivity in the Southern Hemisphere has been found only imperfectly by Otsuka *et al.* (2006) with real GPS data.

Fig. 6 compares TEC time-series showing CIDs propagating northward, eastward and southward, for the main shock (a, c) and the largest aftershock (b, d) of the 2012 North Sumatra earthquake. We used different satellites to realize shallow penetration angle of

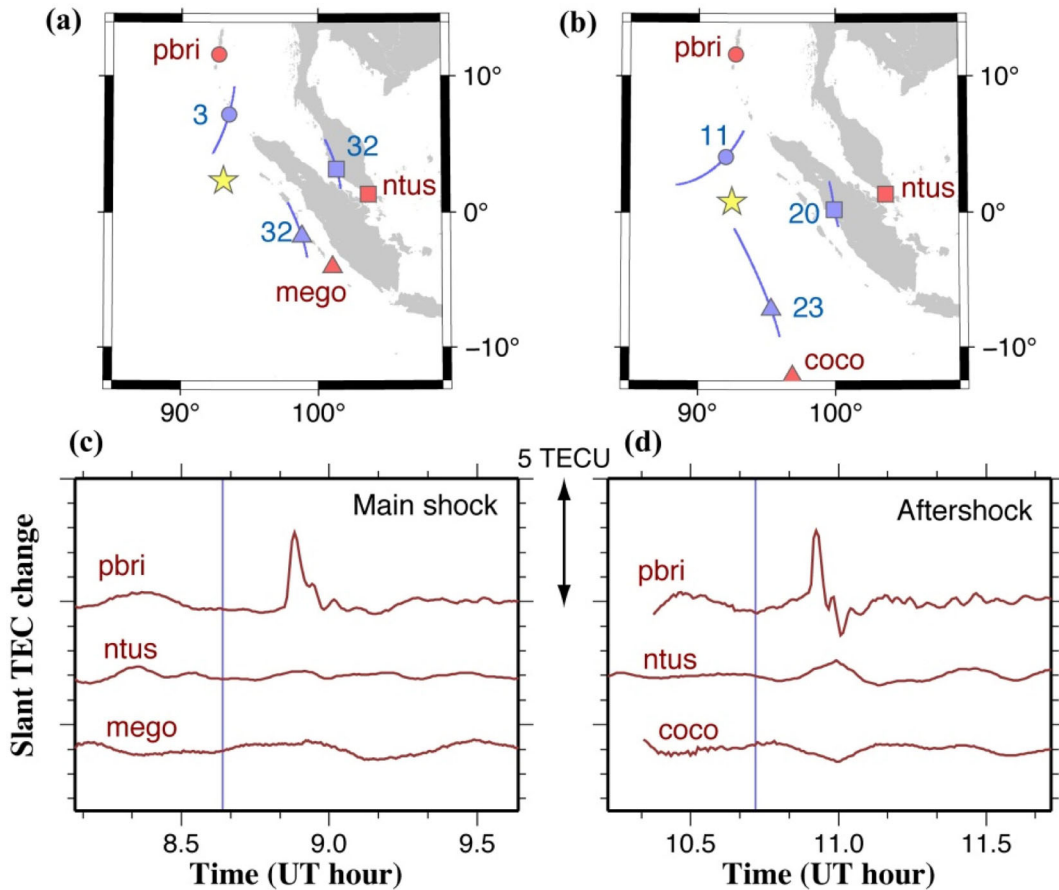


Figure 6. Comparison of the CID of the main shock (a) and the largest aftershock (b) of the 2012 North Sumatra earthquake propagating toward three directions. Their TEC time-series are shown in (c) and (d) for SIPs located to the north (top), east (middle) and south (bottom). We selected satellite-site pairs with geometries of the epicentre (yellow), SIP (blue), GPS station (red) favourable for CID detections (see Fig. 7). Strong CIDs are seen only to the north of the epicentre. Numbers attached to the SIPs in (a, b) are satellite numbers (i.e. TEC data in (c) and (d) are for different pairs of stations and satellites).

LOS to the acoustic wave front (discussed in detail in Section 4.2). In both of the earthquakes, Fig. 6 clearly shows that the strong CIDs are seen only to the north of the epicentre, which is consistent with theoretical expectations.

4 COMPARISON WITH OTHER EARTHQUAKES

4.1 CIDs of 21 earthquakes of various focal mechanisms

Near field CIDs are caused by acoustic waves excited at the surface by coseismic vertical crustal movements. A larger earthquake causes larger crustal deformation and a larger CID (Astafyeva *et al.* 2013). If we know the relationship between them, we could infer earthquake magnitudes from CID amplitudes immediately after acoustic waves arrived at the F region, as early as ~ 7 – 8 min after the earthquake (Astafyeva *et al.* 2011). In the 2011 Tohoku-oki earthquake, the largest tsunami height occurred >20 min later than the earthquake (see, e.g. Mitsui & Heki 2013). In such a case, earthquake magnitudes inferred from CID amplitudes in an early stage may contribute to the disaster mitigation.

Here we collected 21 earthquakes with clear CIDs detected by GPS observations (e.g. GEONET in Japan, SUGAR and IGS networks). Their moment magnitudes range from 6.6 to 9.2. The largest event is the 2004 Sumatra–Andaman earthquake. The smallest earthquake with successful CID detection is the 2007 M_w 6.6

Chuetsu-oki earthquake, central Japan and its TEC data are shown in the Appendix A (Fig. A1). It has the magnitude close to the threshold suggested by Perevalova *et al.* (2014). The 21 earthquakes include two normal fault earthquakes that occurred in the outer rise region of the trenches (2007 January central Kuril, and 2012 December Tohoku-oki), and two strike-slip earthquakes, that is the main shock and the largest aftershock of the 2012 North Sumatra earthquakes. The others are all reverse earthquakes.

Some of the examples have been already reported in past literatures. They include the 2004 Sumatra–Andaman earthquake (Heki *et al.* 2006), the 2011 Tohoku-oki earthquake (e.g. Astafyeva *et al.* 2011), the 2007 Bengkulu earthquake and its largest aftershock (Cahyadi & Heki 2013), the 2006 and 2007 Central Kuril earthquakes (Astafyeva & Heki 2009), the 2004 Hokkaido-Toho-oki earthquake (Astafyeva *et al.* 2009), the 2003 Tokachi-oki earthquake (Heki & Ping 2005), 2004 Kii-Hanto-oki foreshock (Heki & Ping 2005), 2008 Wenchuan earthquake (Afraimovich *et al.* 2010) and 2009 New Zealand and 2006 Tonga earthquakes (Astafyeva *et al.* 2013). Other examples are newly analysed in this study. Their moment magnitudes are taken from the Harvard CMT solutions (www.globalcmt.org). The focal depth ranged from 55 to 6 km (Fig. 9c).

There are three types of earthquake faulting, that is normal, reverse and strike-slip. The first two cause larger vertical crustal movements than the third. Hence, it is important to know both magnitude dependence and focal mechanism dependence of CID

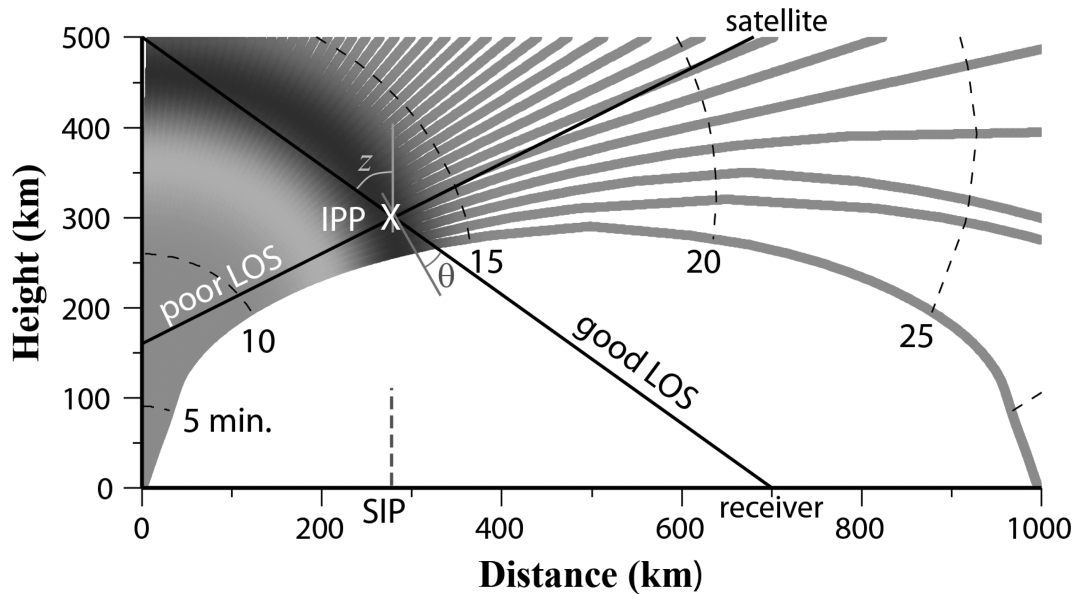


Figure 7. Ray tracing of atmospheric sound waves adopted from Heki & Ping (2005). Black and white wave fronts show the compression and rarefaction part of the wave at 12.5 min after the earthquake. A good LOS captures sharp waveform of the CID but poor LOS does not because it penetrates both black and white parts simultaneously. The SIP and GPS receiver lying on the same side of the epicentre result in small θ , the angle between the CID wave front and the LOS, and clear CID observations. The zenith angle z , on the other hand, does not significantly influence the CID amplitudes. Equal-time contours are shown every 5 min with broken curves.

amplitudes. The 2012 North Sumatra earthquake was the largest strike-slip earthquakes ever recorded, and it is a good opportunity to discuss this point.

Astafyeva *et al.* (2013) also compiled 11 earthquakes with clear CID observations, and investigated the correlation between M_w and CID amplitudes. The three distinct differences of our study from Astafyeva *et al.* (2013) is that (1) we discuss all the three mechanism earthquake while they discussed only thrust (low-angle reverse) earthquakes, (2) number of earthquakes discussed is nearly twofold and (3) we discuss CID amplitude relative to background vertical TEC while they discussed amplitudes of absolute TEC changes. The third point will be discussed in Section 4.3.

4.2 Geometry problem

In these 21 cases, we tried to select the pair of GPS satellite and station showing the largest CID amplitude. Due to the directivity, the SIP should be on the southern/northern side in earthquakes in the Northern/Southern Hemisphere. As shown in the numerical simulation by Rolland *et al.* (2013), the directivity is not so sharp, that is CID amplitudes remain similar for the azimuths within $\sim 20^\circ$ from the main beam direction. Fig. 7 shows ideal geometry of SIPs, epicentres and GPS receivers (see also Calais & Minster (1995) and Afraimovich *et al.* (2001) for the geometry problem). Although the zenith angle of LOS at IPP (z in Fig. 7) governs the ratio between vertical and slant TEC values, it is the CID wave front penetration angle (θ in Fig. 7) that controls the CID amplitude. To achieve small θ , the receiver should be (1) on the same side of the epicentre as the SIP and (2) farther from the epicentre than SIP. Such geometry is important because it enables shallow LOS penetration with the CID wave front.

Actual geometry of epicentre, SIP and GPS stations for the 20 cases are shown in Fig. 8. This figure does not include the 2008 Wenchuan earthquake because the raw GPS data file of the luzh station, China, was not available. Figures in Afraimovich *et al.*

(2010) suggest that its geometric condition was good, and we read the CID amplitude of this earthquake from fig. S1(c) of Astafyeva *et al.* (2013).

The largest factor influencing CID amplitudes would be the earthquake magnitude. In fact, the seismic moment of an $M7$ event and an $M9$ event is different by three orders of magnitude. Apart from the magnitude, two important geometric factors would be the distance between SIP and epicentre and the angle between wave front and LOS (θ in Fig. 7). To isolate magnitude dependence by minimizing the geometric differences, we tried to find the satellite–site pair satisfying the two conditions, that is they should show CID with (1) appearance time not later than 15 min after earthquakes and (2) sharp peaks. The first criterion ensures that SIPs are close to the epicentres and geometric decays are not significant. As shown in fig. 2 of Heki & Ping (2005), CID amplitudes remain the same in this distance range. The second condition is the manifestation of the shallow angle penetration of LOS (small θ in Fig. 7).

Their TEC time-series are shown in Fig. 9. There a simple high-pass filter (subtraction of the best-fitting polynomials with degrees up to six) was applied to raw slant TEC time-series. The ideal geometry may not be always realized. For example, earthquakes sometimes occur in the Nankai Trough off the Pacific coast of SW Japan (e.g. the 2004 Kii-Hanto-oki earthquakes). Their CIDs are difficult to observe with GEONET because few stations exist to the south of the Nankai Trough. In such a case, we have to use a somewhat blunt peak. We did not include an earthquake for which we did not find a pair showing CID appearing within 15 min with a sharp positive peak. For example, we could detect faint CID for the 1999 Chi-Chi earthquake, Taiwan, from SW Japan, but it suffered from attenuation due to large distance from the epicentre and high angle between LOS and wave front. So we did not include it in the discussion. In order to facilitate further investigation, we provide a table in the Appendix A (Table A1) and give key quantities, for example distance between SIP and the epicentre, distance between SIP and the GPS station.

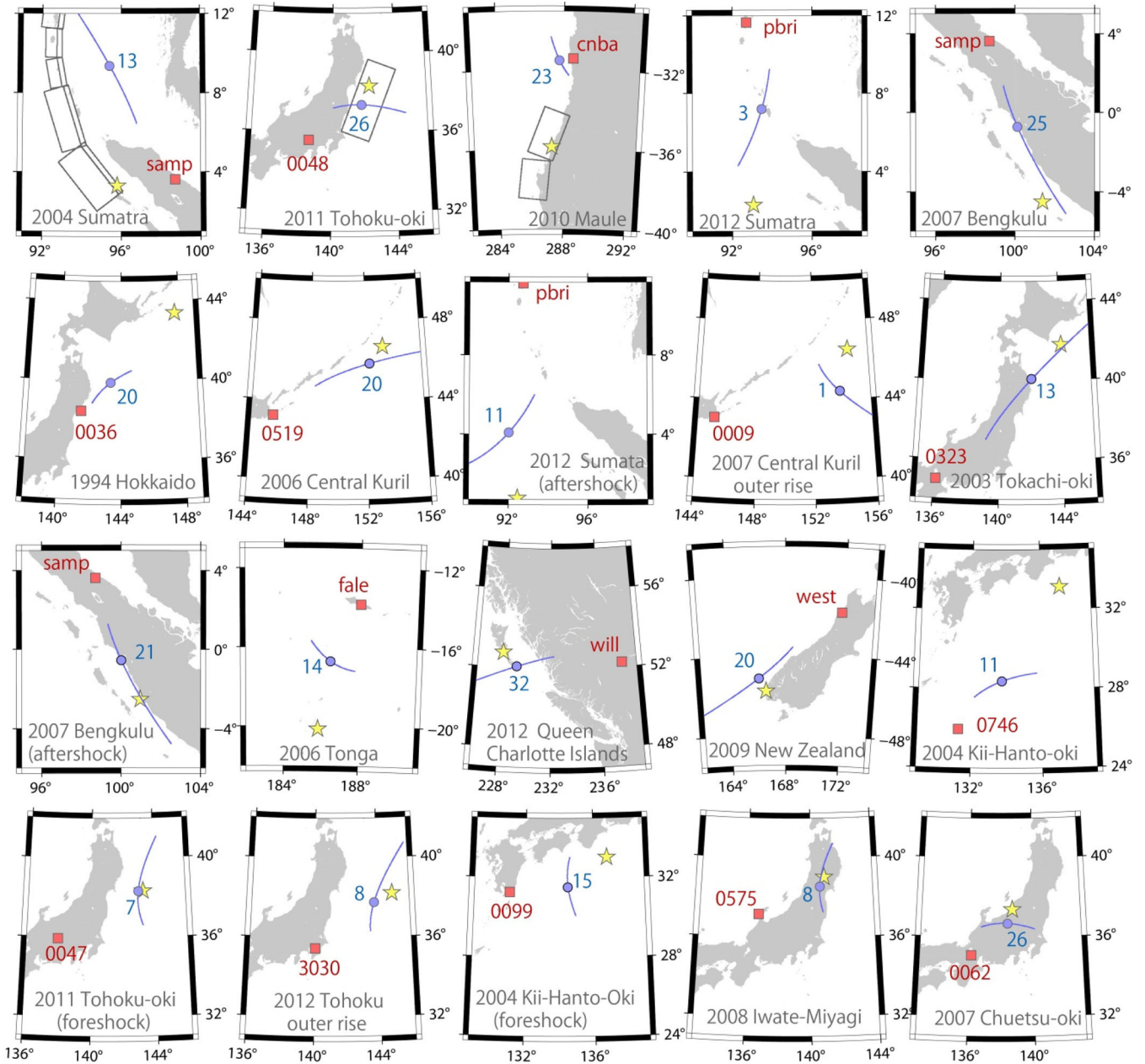


Figure 8. Geometry of epicentre (yellow star), SIP at the time of CID occurrence (blue circle), and GPS receivers (red square) for the 20 examples of CID observations given in Fig. 9. They are displayed in a descending order of magnitudes. Blue curves are SIP trajectories in the time window shown in Fig. 9. For the three M_9 -class earthquakes, approximate shapes of faults are shown by rectangles.

In the case of the 2003 Tokachi-oki earthquake, Satellites 13 and 24 both satisfies the criteria, but the former showed sharper and larger CIDs than the latter (figs 2a,b of Heki & Ping 2005). They showed amplitude difference of a factor of ~ 2 . Here we consider that factor 2 uncertainties always exist in amplitude of every CID example of Fig. 9.

4.3 Earthquake magnitudes and CID amplitudes

The CID amplitudes were derived from time-series shown in Fig. 9 by the following procedure, (1) find the peak TEC value, (2) go back in time from the peak by 1.5 min and read TEC values and (3) calculate the difference between the two TEC values. Astafyeva *et al.* (2013) compared ‘absolute’ CID amplitudes among earthquakes.

However, coseismic uplifts excite waves in neutral atmosphere, and it would be therefore more natural to normalize CID amplitudes with the electron densities in the F region. Because the electron density at a particular height is not always available, we used vertical TEC as a factor to normalize CID amplitudes.

We obtained the background vertical TEC at the time and place where the CIDs were detected using Global Ionospheric Maps (GIM; Mannucci *et al.* 1998). In Fig. 10 we compare ‘relative’ CID amplitudes, that is those normalized with the background vertical TEC. In Fig. 9, CID of the 2012 North Sumatra aftershock (M_w 8.2) show slightly larger amplitude than that of the 2010 Maule earthquake (M_w 8.8). However, after normalization with background vertical TEC (51.4 TECU and 6.0 TECU, respectively), the relative amplitude of the latter exceeds the former. For latitude bands with

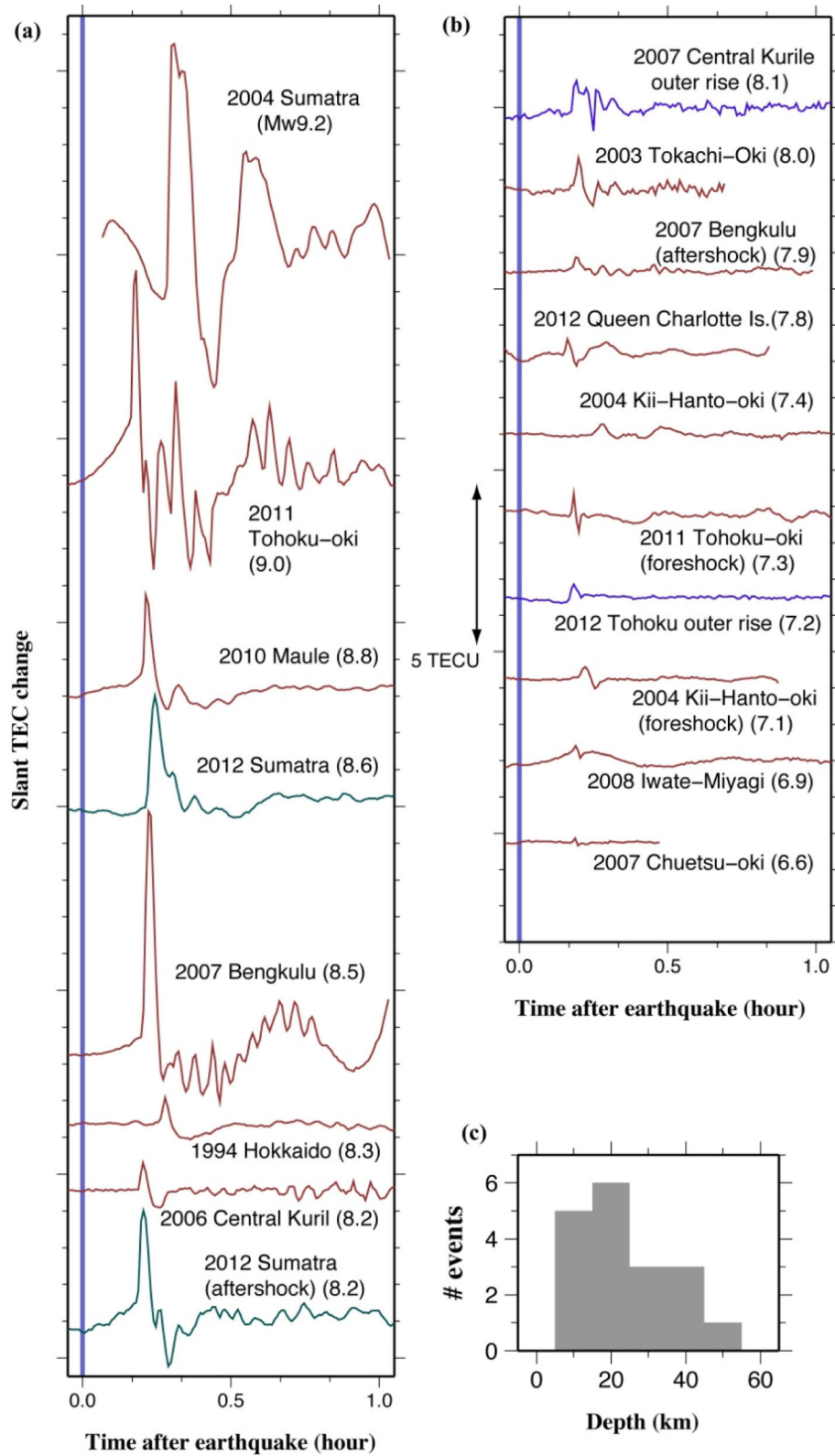


Figure 9. TEC time-series showing 20 examples of CID observations in the time window from -0.5 to 1.05 hr for earthquakes with magnitudes 9.2 – 8.2 (a) and 8.1 – 6.6 (b). Moment magnitudes are shown within the parentheses. Colours of the curves show reverse (red), normal (blue) and strike-slip (green) mechanisms. Distribution of the focal depths is shown as a histogram in (c).

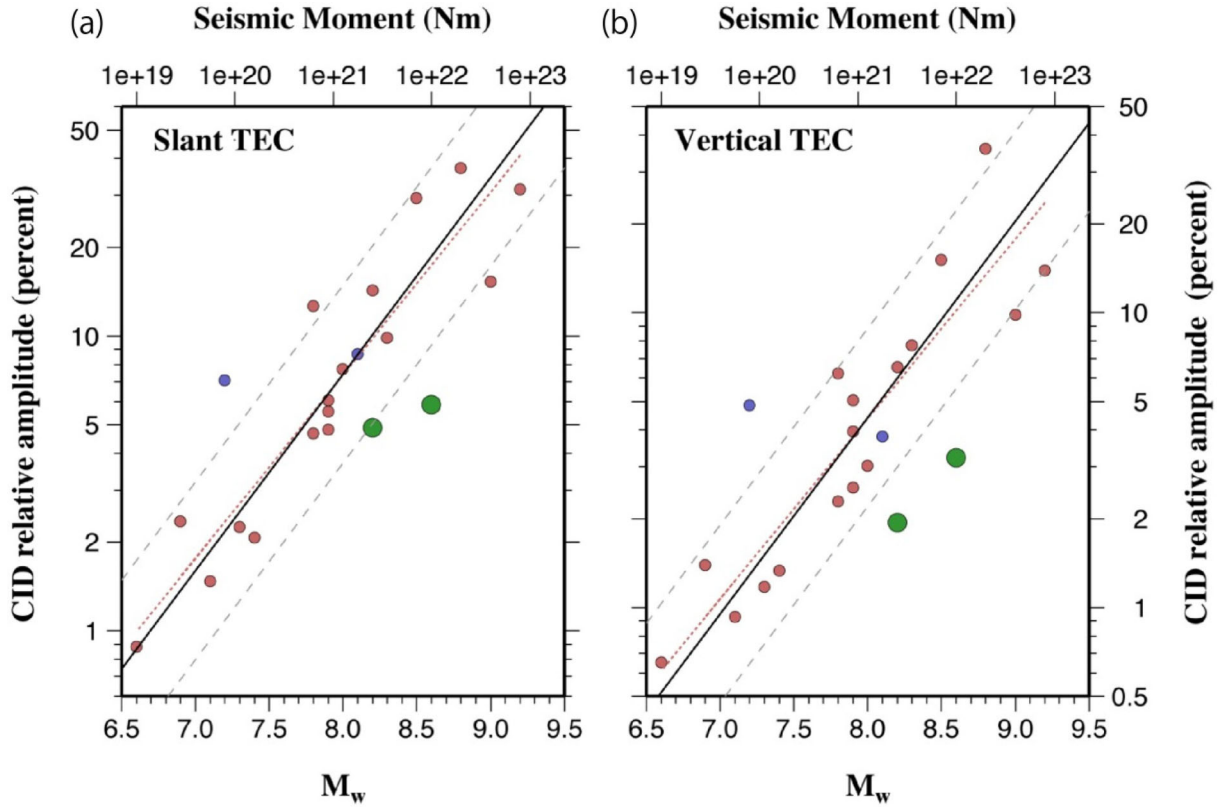


Figure 10. Comparison of moment magnitudes of the 21 earthquakes shown in Figs 8, 9, and the Wenchuan earthquake from Astafyeva *et al.* (2013), with their relative CID amplitudes in slant (a) and vertical (b) TEC. CID amplitudes in both (a) and (b) are normalized by the background vertical TEC. Colours of the symbols show the faulting mechanisms, that is red (reverse), blue (normal) and strike-slip (green). The black line indicates the best-fitting line with the fixed slope of 2/3, that is the difference in 3 of M_w corresponds to the two orders of difference in CID amplitudes. Dashed lines indicate uncertainties of factor two differences coming from non-ideal LOS geometry. The red dotted line indicates the best-fitting line with both slope and offset inferred by linear regression for the 17 data of reverse earthquakes. CID amplitudes of strike-slip earthquakes (green) show somewhat smaller values than other earthquakes.

insufficient ground station coverage, GIM sometimes gives unrealistic values. For example, the vertical TEC at the time of the 2009 July 15 New Zealand earthquake (9:22 UT) is ~ 1.4 TECU according to GIM, but we revised it to ~ 4.1 TECU by analysing GPS data of the ‘west’ station following Astafyeva & Heki (2011).

One may think it necessary to convert the CID amplitudes in slant TEC to vertical TEC. As shown in Fig. 7, it is the incident angle θ rather than the zenith angle z that governs the CID amplitudes, conversion to vertical TEC is unnecessary. We demonstrate this by comparing Figs 10(a) and (b), where slant TECs are better correlated with M_w than vertical TECs.

It would be reasonable to assume that the relative CID amplitude may scale with the coseismic crustal uplift of an earthquake (e.g. Astafyeva *et al.* 2013). In Appendix A (Fig. A2), we show that the uplift obeys different scaling laws with earthquake magnitudes for relatively large ($M > 7$) and small ($M < 7$) events. Because CIDs appear only after larger earthquakes, we considered CID amplitudes would obey the same scaling law as the large events, that is CID amplitudes increase by two orders of magnitude as M_w increases by three (i.e. the slope is 2/3). In Fig. 10(a), where we used the logarithmic vertical axis, data are distributed roughly around a line with the slope of 2/3. We express the relationship between the moment magnitude and the relative CID amplitude (unit: percent) as follows,

$$\log_{10}(\text{CID amplitude}) = a(M_w - 8.0) + b. \quad (1)$$

The offset b is the common logarithm of the relative CID amplitude in percent of an M_w 8 event. In the best-fitting line inferred from reverse earthquakes (dotted line in Fig. 10a), the slope a was 0.621 with the 1σ uncertainty of 0.064 and b was estimated as 0.867 with the 1σ uncertainty of 0.045. Because the slope coincides with 2/3 within 1σ , we fixed a to 2/3 (solid line in Fig. 10a) and estimated b as 0.871 with the 1σ uncertainty of 0.044. The overall picture (slope and outliers) remains the same even with the vertical TEC (Fig. 10b).

As discussed in Section 5.2, we consider that observed CID amplitudes may have factor 2 uncertainties, and we indicate it with two dashed lines. Fig. 10(a) showed same characteristic for some of the earthquakes, that is there are a few data lying significantly beyond these lines. For example, the 2012 Tohoku outer rise earthquake and the 2012 North Sumatra earthquakes deviate upward and downward, respectively. The former earthquake is composed of two events of comparable magnitude, a reverse faulting deep within the subducting oceanic plate and a shallow normal faulting near the surface. The former contributes little to the coseismic crustal movements, and the shallow epicentral depth of the latter (~ 6 km, and this is the shallowest in the 21 earthquakes studied here) might be responsible for the relatively large CID.

The latter earthquakes (the 2012 North Sumatra earthquakes) negatively deviate from the general trend. These deviations are consistent with the smaller vertical crustal movements of strike-slip earthquakes than dip-slip events (Fig. A2). We would need more CID examples of strike-slip earthquakes to discuss statistical

significance of their small CIDs. In fact, strike-slip earthquakes are scarcely large enough to disturb the ionosphere. For example, the largest strike-slip event in Japan that occurred after the deployment of the dense GPS network is the 1995 January Southern Hyogo Prefecture (Kobe) earthquake (M_w 6.9), for which we could not detect CID.

If we could measure the CID amplitude with factor-two uncertainty, the inferred relationship in Fig. 10(a) suggests that we could determine M_w with an uncertainty of ± 0.45 about 10 min after the earthquake. This is useful for early warning in a region where tsunamis arrive at the coast later than acoustic waves arrive at the ionospheric F region, and this is the case for the Pacific coast of NE Japan.

Areal extent of strong CID appearance would be another measure to infer M_w , and this is one of the future issues to be studied. No systematic dependence of CID amplitudes on the focal depth was seen (except the large CID amplitude for the shallowest event). The 2006 May Tonga (~ 55 km) and the 2013 September Tokachi-oki (~ 45 km) earthquakes have the deepest epicentres, but their CIDs do not show significant negative deviations from the rest. Depths to the centre of the fault might better correlate with CID amplitudes. The correlation between the CID amplitudes and maximum coseismic vertical crustal movements (available in Table A1) was less clear than in Fig. 10. Other quantities, for example vertical movements integrated two-dimensionally over the surface, might show clearer correlation.

5 CONCLUSIONS

This research provides the comprehensive study of multiple aspects of CIDs, included velocity signal propagation (the observed velocity is ~ 1 km s $^{-1}$, suggested as acoustic wave), oscillation signal (~ 3.7 mHz), time-series and their azimuthal asymmetry of propagation which is the first proof of phenomena in the Southern Hemisphere.

Another important result of this research is scaling law which represents relation between normalized TEC and moment magnitude of the earthquake. The relation between TEC and the moment magnitude shows that strike slip earthquakes tend to negatively deviate from this law. This is useful for early warning system tsunami with the arrival time later than the acoustic wave signals (for example Pacific coast of NE Japan). This approach is beneficial also for a part of Indonesia where the tsunami takes more time to reach shores than does the acoustic wave to reach the ionospheric F region. Deeper researches should be done to make the law more accurate, especially for adding more strike slip earthquakes.

ACKNOWLEDGEMENTS

We thank Paramesh Banerjee, Earth Observatory of Singapore and Danny Hilman Natawidjaja, LIPI, for providing the RINEX files of the SUGAR network on the earthquake day. KH thanks Yuta Mitsui, Shizuoka University, for discussion on the scaling law of CID amplitudes. Constructive reviews by the two referees improved the quality of the paper. MNC is supported by the Indonesian government fellowship (DIKTI scholarship).

REFERENCES

Afraimovich, E.L., Perevalova, N.P., Plotnikov, A.V. & Uralov, A.M., 2001. The shock-acoustic waves generated by earthquakes, *Ann. Geophys.*, **19**, 395–409.

- Afraimovich, E.L., Feng, D., Kiryushkin, V.V. & Astafyeva, E.I., 2010. Near-field TEC response to the main shock of the 2008 Wenchuan earthquake, *Earth Planets Space*, **62**, 899–904.
- Astafyeva, E. & Heki, K., 2009. Dependence of waveform of near-field coseismic ionospheric disturbances on focal mechanisms, *Earth Planets Space*, **61**, 939–943.
- Astafyeva, E. & Heki, K., 2011. Vertical TEC over seismically active region during low solar activity, *J. Atm. Terr. Phys.*, **73**, 1643–1652.
- Astafyeva, E., Heki, K., Kiryushkin, V., Afraimovich, E. & Shalimov, S., 2009. Two-mode long-distance propagation of coseismic ionosphere disturbances, *J. geophys. Res.*, **114**, A10307, doi:10.1029/2008JA013853.
- Astafyeva, E., Lognonné, P. & Rolland, L., 2011. First ionosphere images for the seismic slip of the Tohoku-oki Earthquake, *Geophys. Res. Lett.*, **38**, L22104, doi:10.1029/2011GL049623.
- Astafyeva, E., Shalimov, S., Olshanskaya, E. & Lognonné, P., 2013. Ionospheric response to earthquakes of different magnitudes: larger quakes perturb the ionosphere stronger and longer, *Geophys. Res. Lett.*, **40**, 1675–1681.
- Cahyadi, M.N. & Heki, K., 2013. Ionospheric disturbances of the 2007 Bengkulu and the 2005 Nias earthquakes, Sumatra, observed with a regional GPS network, *J. geophys. Res.*, **118**, 1–11.
- Calais, E. & Minster, J.B., 1995. GPS detection of ionospheric perturbations following the January 17, 1994, Northridge earthquake, *Geophys. Res. Lett.*, **22**, 1045–1048.
- Choosakul, N., Saito, A., Iyemori, T. & Hashizume, M., 2009. Excitation of 4-min periodic ionospheric variations following the great Sumatra-Andaman earthquake in 2004, *J. geophys. Res.*, **114**, A10313, doi:10.1029/2008JA013915.
- Heki, K., 2011. Ionospheric electron enhancement preceding the 2011 Tohoku-Oki earthquake, *Geophys. Res. Lett.*, **38**, L17312, doi:10.1029/2011GL047908.
- Heki, K. & Enomoto, Y., 2013. Preseismic ionospheric electron enhancements revisited, *J. geophys. Res.*, **118**, 6618–6626.
- Heki, K. & Ping, J.-S., 2005. Directivity and apparent velocity of the coseismic ionospheric disturbances observed with a dense GPS array, *Earth planet. Sci. Lett.*, **236**, 845–855.
- Heki, K., Otsuka, Y., Choosakul, N., Hemmakorn, N., Komolmis, T. & Maruyama, T., 2006. Detection of ruptures of Andaman fault segments in the 2004 great Sumatra earthquake with coseismic ionospheric disturbances, *J. geophys. Res.*, **111**, B09313, doi:10.1029/2005JB004202.
- Klobuchar, J., 1987. Ionospheric time-delay algorithms for single-frequency GPS users, *IEEE Trans. Aerospace Electr. Sys.*, **3**, 325–331.
- Mannucci, A.J., Wilson, B.D., Yuan, D.N., Ho, C.H., Lindqwister, U.J. & Runge, T.F., 1998. A global mapping technique for GPS-derived ionospheric total electron content measurements, *Radio Sci.*, **33**, 565–582.
- Meng, L., Ampuero, J.-P., Stock, J., Duputel, Z., Luo, Y. & Tsai, V.C., 2012. Earthquake in a maze: compressional rupture branching during the 2012 M_w 8.6 Sumatra Earthquake, *Science*, **337**, 724–726.
- Mitsui, Y. & Heki, K., 2013. Scaling of early afterslip velocity and possible detection of tsunami-induced subsidence by GPS measurements immediately after the 2011 Tohoku-Oki earthquake, *Geophys. J. Int.*, **195**, 238–248.
- Nishida, K., Kobayashi, N. & Fukao, Y., 2000. Resonant oscillation between the solid earth and the atmosphere, *Science*, **287**, 2244–2246.
- Okada, Y., 1992. Internal deformation due to shear and tensile faults in a half-space, *Bull. seism. Soc. Am.*, **82**, 1018–1040.
- Otsuka, Y. *et al.*, 2006. GPS detection of totalelectron content variations over Indonesia and Thailand following the 26 December 2004 earthquake, *Earth Planets Space*, **58**(2), 159–165.
- Ozeki, M. & Heki, K., 2010. Ionospheric holes made by ballistic missiles from North Korea detected with a Japanese dense GPS array, *J. geophys. Res.*, **115**, A09314, doi:10.1029/2010JA015531.
- Perevalova, N.P., Sankov, V.A., Astafyeva, E.I. & Zhupityaeva, A.S., 2014. Threshold magnitude for ionospheric TEC response to earthquakes, *J. Atmos. Solar-Terrestrial Phys.*, **108**, 77–90.
- Rideout, W. & Coster, A., 2006. Automated GPS processing for global total electron content data, *GPS Solut.*, **10**, 219–228.

Rolland, L.M., Lognonné, P. & Munekane, H., 2011a. Detection and modelling of Rayleigh wave induced patterns in the ionosphere, *J. geophys. Res.*, **116**, A05320, doi:10.1029/2010JA016060.

Rolland, L.M., Lognonné, P., Astafyeva, E., Kherani, E.A., Kobayashi, N., Mann, M. & Munekane, H., 2011b. The resonant response of the ionosphere imaged after the 2011 off the Pacific coast of Tohoku earthquake, *Earth Planets Space*, **63**, 853–857.

Rolland, L.M., Vergnolle, M., Nocquet, J.-M., Sladen, A., Dessa, J.-X., Tavakoli, F., Nankali, H.R. & Cappa, F., 2013. Discriminating the tectonic and non-tectonic contributions in the ionospheric signature of the 2011, M_w 7.1, dip-slip Van earthquake, Eastern Turkey, *Geophys. Res. Lett.*, **40**, 2518–2522.

Saito, A. *et al.*, 2011. Acoustic resonance and plasma depletion detected by GPS total electron content observation after the 2011 off the Pacific coast of Tohoku Earthquake, *Earth Planets Space*, **63**, 863–867.

Sakai, T., 2005. Bias error calibration for observing ionosphere by GPS network, *J. Inst. Electron. Inf. Commun. Eng.*, **J88-B**, 2382–2389 (in Japanese).

Shinagawa, H., Iyemori, T., Saito, S. & Maruyama, T., 2007. A numerical simulation of ionospheric and atmospheric variations associated with the Sumatra earthquake on December 26, 2004, *Earth Planets Space*, **59**, 1015–1026.

Tahira, M. 1995. Acoustic resonance of the atmospheric at 3.7 mHz, *J. Atmos. Sci.*, **52**, 2670–2674.

Tanimoto, T., Heki, K. & Artru-Lambin, J., 2014. Interaction of solid Earth, atmosphere and ionosphere, *Treatise on Geophysics*, Elsevier, in press.

Tsugawa, T., Saito, A., Otsuka, Y., Nishioka, M., Maruyama, T., Kato, H., Nagatsuma, T. & Murata, K.T., 2011. Ionospheric disturbances detected by GPS total electron content observation after the 2011 off-the-Pacific coast of Tohoku Earthquake, *Earth Planets Space*, **63**, 875–879.

Yue, H., Lay, T. & Koper, K.D., 2012. En échelon and orthogonal fault ruptures of the 11 April 2012 great intraplate earthquakes, *Nature*, **490**, 245–249.

APPENDIX A

Table A1 gives quantities which might be useful for further analyses of the near-field CIDs discussed in this paper. Fig. A1 shows the high-pass filtered slant TEC time-series, distance–time diagram and the map view of the GPS sites and SIPs for the smallest earthquake whose near-field CID has been clearly observed (M_w 6.6 2007 Chuetsu-oki earthquake in Central Japan). Fig. A2 shows the relationship between the largest uplifts and moment magnitudes of thrust and strike-slip earthquakes. The events with magnitudes exceeding 7 seem to obey a similar scaling law as the relative CID amplitudes (Fig. 10).

Table A1. Twenty-one earthquakes with clear CIDs discussed in the paper.

Year/Month/Day	Earthquake	Time		Epicentre		SIP		Maximum		GIM-VTEC (TECU)	D1 (km)	D2 (km)	Depth (km)	Uplift (m)	Mechanism
				Long. (°E)	Lat. (°N)	Long. (°E)	Lat. (°N)	CID (TECU)	Sat. Stn.						
2004/12/26	Sumatra-Andaman	9.2	1.25	95.854	3.316	95.412	9.372	6.59	13 samp	20.95	320	671	30	3.4	R
2011/03/11	Tohoku-oki	9.0	5.90	142.372	38.297	141.868	37.378	4.22	26 0048	27.67	452	111	24	5.0	R
2010/02/27	Maule	8.8	6.80	-72.733	-35.909	-72.268	-31.488	2.24	23 cnba	6.04	514	492	35	3.0	R
2012/04/11	North Sumatra	8.6	8.80	93.063	2.311	93.475	7.185	2.62	3 pbri	44.94	1031	541	22.9	2.1	S
2007/09/12	Sumatra Bengkulu	8.5	11.40	101.374	-4.520	100.122	-0.716	6.15	25 samp	20.99	947	443	34	1.3	R
1994/10/04	Hokkaido-toho-oki	8.3	13.50	147.321	43.773	143.325	39.881	0.68	20 0036	6.89*	770	545	24	2.0	R
2006/11/15	Central Kuril	8.2	11.40	153.230	46.607	152.252	45.836	0.73	20 0519	5.16	716	114	30.3	1.0	R
2012/04/11	North Sumatra (after)	8.2	10.90	92.452	0.773	92.006	4.083	2.51	11 pbri	51.39	1200	369	16	1.2	S
2007/01/13	Central Kuril outer rise	8.1	4.60	154.455	46.272	153.830	44.411	0.63	1 0009	7.27	819	213	10	0.7	N
2003/09/25	Tokachi-oki	8.0	20.00	143.904	41.775	142.098	40.068	0.77	13 0323	9.99	1015	243	45	0.7	R
2007/09/13	Sumatra Bengkulu (after)	7.9	0.00	100.906	-2.506	100.010	-0.549	0.36	21 samp	7.56	720	238	10	0.6	R
2006/05/03	Tonga	7.9	15.44	-174.164	-20.130	-173.530	-16.716	0.35	14 fale	5.79	734	383	55	0.6	R
2008/05/12	Wenchuan	7.9	6.47	103.364	30.986	105**	30**	1.04	22 luzh	18.73	—	191	13	4.7	R
2012/10/28	Queen Charlotte Islands	7.8	3.24	-132.131	52.742	-130.777	52.076	0.16	32 will	8.72	678	118	17.5	2.3	R
2009/07/15	New Zealand	7.8	9.37	166.577	-45.750	166.000	-45.000	0.52	20 west	4.10***	751	94	12	1.5	R
2004/09/05	Kii-hanto-oki	7.4	15.12	136.608	33.062	133.736	28.377	0.30	11 0746	14.50	940	587	44	0.7	R
2011/03/09	Tohoku-oki (fore)	7.3	2.92	142.840	38.440	142.992	38.316	0.61	7 0047	27.18	517	19	8	0.8	R
2012/12/07	Tohoku outer rise	7.2	8.47	144.090	37.889	143.752	37.747	0.50	8 3030	7.13	451	34	6	0.3	N
2004/09/05	Kii-hanto-oki (fore)	7.1	10.20	136.608	33.062	134.503	31.533	0.29	15 0099	20.08	558	261	38	0.3	R
2008/06/13	Iwate-Miyagi	6.9	23.90	140.678	39.122	140.598	38.554	0.23	8 0575	9.91	410	63	8	1.2	R
2007/07/16	Chuetsu-oki	6.6	1.40	138.469	37.576	138.399	36.703	0.12	26 0062	13.41	345	97	17	0.3	R

Note. (fore): foreshock, (after): largest aftershock, Time: approximate time of the CID appearance.

D1: distance between epicentre and GPS station, D2: distance between epicentre and SIP.

Mechanisms are R (revers), N (normal) or S (strike-slip).

Maximum uplift was calculated either using published fault parameters, or modeling fault parameters after Fig. A2.

*GIM from the same day in 2005 (11 years after the earthquake), **approximate SIP coordinates from Afraimovich *et al.* [2010].

***calculated using data at “west”.

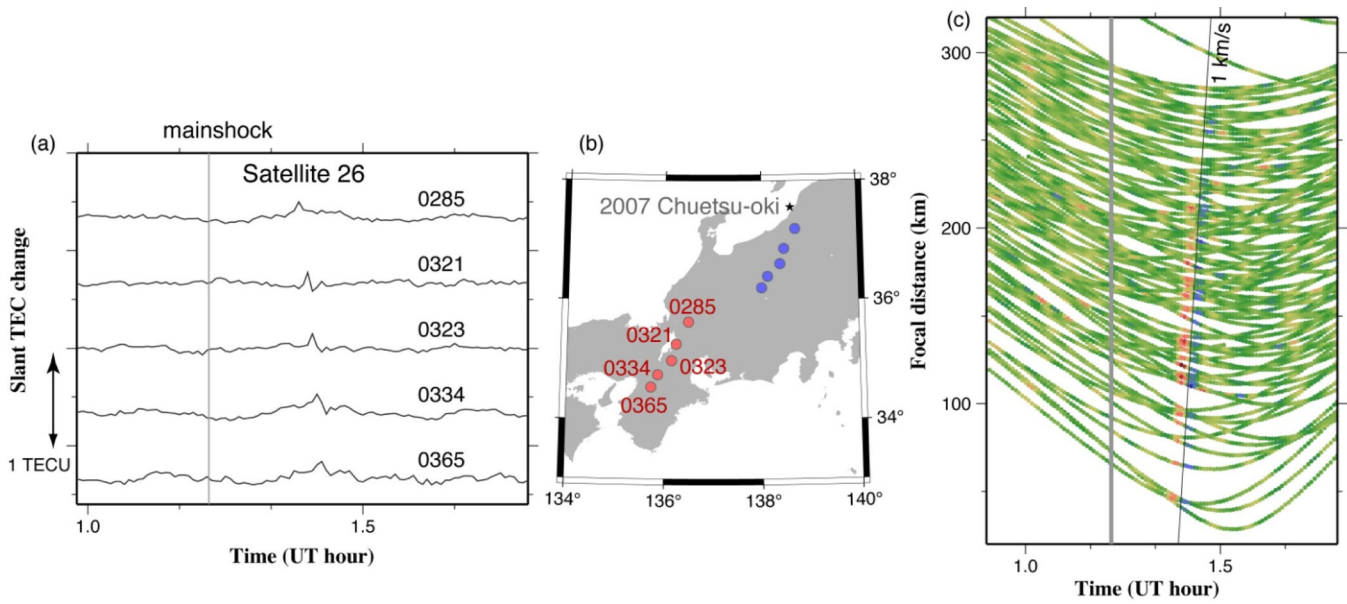


Figure A1. CID of the 2007 July 16 Chuetsu-oki earthquake (M_w 6.6) observed with Satellite 26. This was the smallest earthquake whose CID clearly detected with GPS. Time-series of TEC changes at five stations (a), positions of GPS stations and their SIPs (b), and traveltime diagram drawn using the same wavelet analyses as in Fig. 4(c).

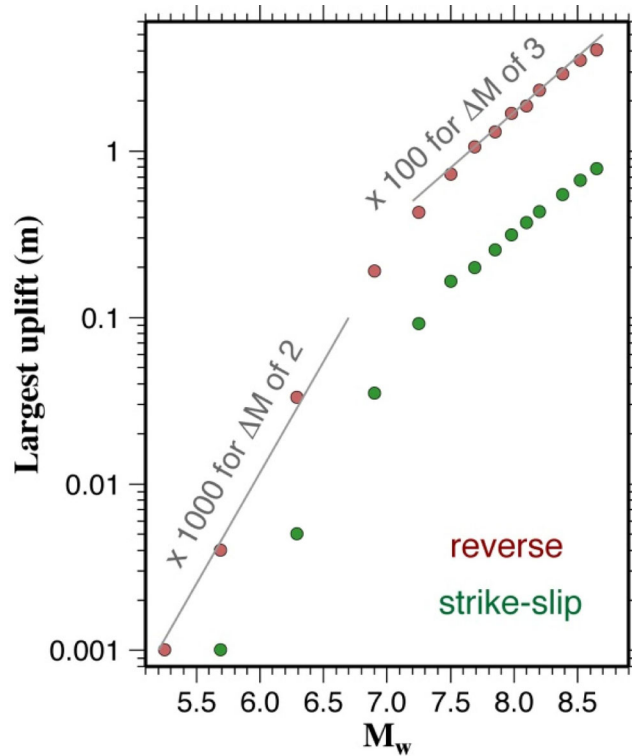


Figure A2. Relationship between maximum uplift and moment magnitude for shallow angle thrust (dip angle: 15° , depth: 25 km, rigidity: 50 GPa) earthquakes (red circles). Length of the fault was assumed to be twice as long as width, and the dislocation was given to realize the constant stress drop (3 MPa). They seem to obey two different scaling laws for smaller and larger events. Green circles show those for strike-slip earthquakes (for larger earthquakes, upper edge of the fault was assumed to coincide with the surface).

APPENDIX B

In Fig. B1, we plot space weather indices over the one month period before and after the 2012 North Sumatra earthquake. Geomagnetic condition on the earthquake day was moderately active.

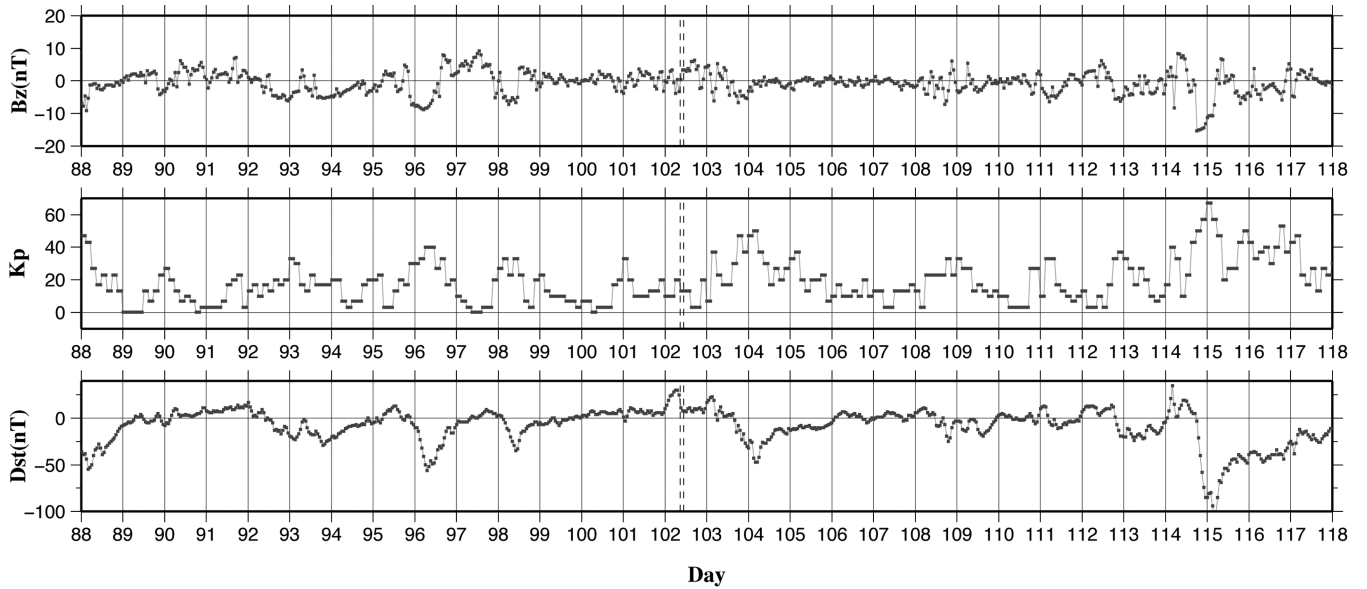


Figure B1. Space weather data, that is B_z (north–south component of the interplanetary magnetic field), K_p index, and the D_{st} index, over 1 month time windows including the 2012 North Sumatra earthquakes (day 102, vertical dashed lines). Data are taken from NASA omniweb (omniweb.gsfc.nasa.gov).